Progress In Electromagnetics Research, PIER 18, 105–125, 1998

CHARACTERIZATION OF A TRANCEIVING ANTENNA CONCEPT FOR MICROWAVE HEATING AND THERMOMETRY OF SUPERFICIAL TUMORS

S. Jacobsen, A. Murberg

Institute of Mathematical and Physical Sciences
Applied Physics Group, Physics Department
University of Tromsø
N-9037 Tromsø, Norway

P. R. Stauffer

Department of Radiation Oncology
University of California
San Francisco, CA, USA

1. INTRODUCTION

Hyperthermia is currently being used as an adjunct to radiation therapy and chemotherapy of superficial malignancies [1–3]. However, use of hyperthermia is limited despite reported efficacy in both laboratory and clinical application. This phenomenon is due primarily to lack of efficient heating applicators capable of heating large volume (or area) tumors that typically require adjuvant therapy up to therapeutic

temperatures. In addition, the lack of reliable temperature feedback control systems which can be implemented noninvasively limits the options of clinicians during treatment.

Devices designed to heat these superficially localized (< 2–3 cm depth), and often large area disease sites, must satisfy criteria associated with tissue heterogeneities, conformity to body contours, thermometry, patient safety, and production cost.

Physiological and anatomical factors increase the complexity of achieving acceptable performance of microwave applicators. Early microwave hyperthermic antenna designs had a tendency to be bulky and awkward to couple to the human body. A variety of more or less adequate printed-circuit applicator designs have been proposed for hyperthermia to improve conformity to the body surface [4–9]. This includes rectangular, circular, ring, spiral, and other more advanced patch radiator shapes.

During the 1990's a new generation of specialized applicators have been developed for superficial heating [10–12]. The applicators present the following properties: i) Lightweight and at least partly flexible for fixation over a tumor, ii) effective power deposition pattern extending to the periphery of the aperture, iii) relatively simple and low-cost construction. One aspect of printed antennas is the observed electric field component normal to the applicator face which has been reported to dominate in the reactive nearfield of the antenna. Maxwell's equations imply that the normal component of the electric flux intensity at the interface between fat and muscle must drop in inverse proportion according to the boundary conditions. Because of the higher relative permittivity of muscle compared to fat/skin, significantly more energy may be deposited in the low-loss fat layer than in the high-loss muscle [13]. This problem has been addressed in the proposed design (Sections 2 and 3).

One issue discussed in plenum at the 7th International Congress on Hyperthermic Oncology in Rome 1996, was the importance of noninvasively establishing temperature profiles during hyperthermic therapy. Several methods, including pulse-echo ultrasound [14], electrical impedance tomography [15–16], active microwave imaging [17], magnetic resonance imaging [18], and microwave radiometry are under investigation. In this paper the feasibility of integrating the latter method into a dual transmit/receive antenna configuration will be investigated.

A number of research groups have during the last 25 years explored the use of microwave radiometry for noninvasive monitoring of subcutaneous tissue temperature. The radiometers applied are operated at low gigaheartz frequencies (1–4 GHz) with waveguide antennas [19], small loop antennas [20] or more sophisticated antenna designs [21].

In radiometry, the tradeoffs between antenna size related to spatial resolution and penetration depth are of primary importance. Antennas with a large effective aperture area have a larger depth of measurement sensitivity compared to more omnidirectionally (small) radiating antennas; i.e. the maximum penetration depth is constrained to be less than far field radiation from an infinitely large antenna. In practice the effective depth of sensing depends on aperture size, geometric construction, sense frequency, and dielectric properties of the medium [22]. This was verified experimentally in [23] where measured penetration distances were compared to theoretical plane wave values.

In addition, an antenna can only sense regions or detect objects of a size comparable to its dimension (also a function of depth); hence detectability is inversely proportional to the antenna's own size although improved recognition to some extent can be obtained by overlapping antenna apertures [24] or correlation techniques [25].

The ability to deliver/receive EM-energy to/from a lossy dielectric load is strongly related to antenna input impedance. For resonant mode antennas, EM coupling with a biological medium is adequate only in a small resonance band. Although resonant antennas are efficient, there is a tradeoff between their resonance properties and the stability of their heating patterns for variable tissue loading. Excellent EM coupling with biological tissue over a wide frequency range can, however, be obtained by traveling wave radiators which are generally broadband. Experimental and clinical tests have proven that these type of applicators provide superior performance compared to resonant mode antennas [7], [26]. Presently, a microstrip spiral antenna concept is investigated for it usefulness as a broadband receiver to fit the following set of performance criteria.

The thermometric antenna should be directive (high gain in the boresight direction ($\theta = 0^o$) and characterized by a narrow main lobe) to receive thermal radiation only from tissue directly below the sensing antenna and not from tissue which may be heated by adjacent transmitting antennas. A high gain in the boresight direction also makes the antenna more sensitive to weak thermal noise levels and hence in-

creases the sensing depth of thermal noise signals. Furthermore, in a transmitting mode, the applicator should radiate out to the periphery of the aperture to obtain large surface area hyperthermia. This latter feature implies the need for a broad main lobe or a split beam configuration.

From the requirements listed above, it is obvious that one applicator can not satisfy the two divergent features simultaneously. This calls for a design where two different antennas (one for transmitting and one for receiving) are combined to yield a more optimized solution. The challenge is to obtain a practical dual antenna design with a minimum of etching overlap and EM-interference between the transmitting, receiving, and feedline components.

2. METHODS

2.1 Applicator design and characteristics

Figure 1 illustrates the antenna configuration and the coordinate system. Starting with the receiving spiral antenna, the antenna arm is described by the Archimedean spiral function $r = \Gamma\phi_s$ (Γ:spiral constant, ϕ_s:winding angle). Apart from Γ, the strip width w, the substrate permittivity ϵ_{rs}, and substrate thickness d are degrees of freedom in the design.

It is desirable for the receiving antenna to satisfy the following performance characteristics: i) The applicator diameter ($d_s \simeq 3.5$ cm) should be small to yield good thermometric spatial resolution, ii) the spiral should be relatively loosely wound to prevent excessive capacitive coupling between adjacent turns, which tends to increase the spiral input impedance, iii) the spiral should be an efficient (return loss < -10 dB) receiving antenna over a wide frequency range in order to be operable at multiple frequency bands [23].

After some preliminary design effort with feedback corrections, the following parameter values were used: Spiral constant $\Gamma = 0.035$ cm, strip width $w = 0.5$ mm, range of winding angle ϕ_s, $9.07 \text{ rad} \leq \phi_s \leq 35.7$ rad, substrate thickness and permittivity $d = 0.8$ mm, and $\epsilon_{rs} = 2.53$, respectively.

A simple and efficient technique to remove residual power not radiated in the resonance zone along the spiral, is to place a ring of absorbing material at the truncated edge [27] or terminate the spiral with a 50 Ω load. Here the latter variant is used and allows absorption of

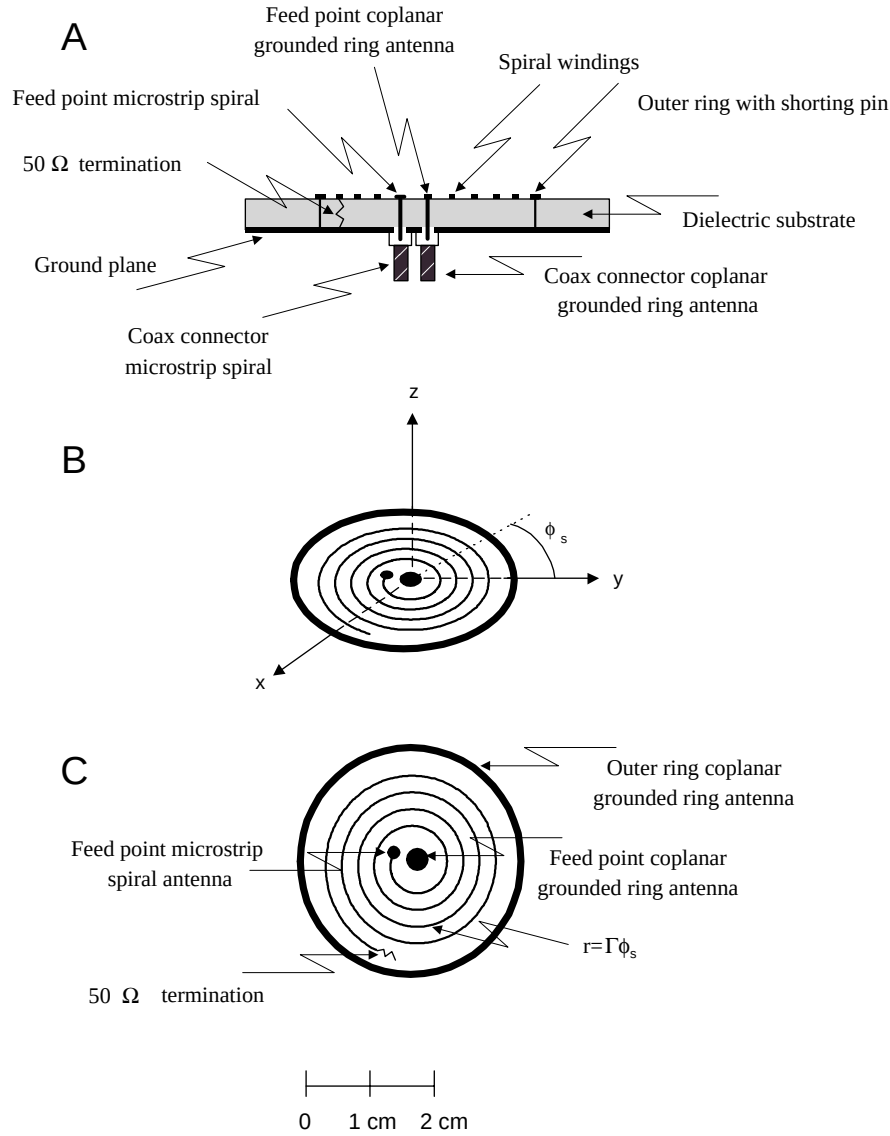

Figure 1. Schematic representation of tranceiving antenna concept. (A) Side view, (B) perspective view with coordinate system, (C) top view with printed microstrips.

residual power, which otherwise has a tendency to reflect back along the spiral and radiate in unwanted modes, resulting in deteriorated (asymmetric) radiation patterns. The spiral antenna is also sensitive to the electrical properties of the lossy medium in direct contact with the surface. Lee et al. [8] handled this problem by introducing impedance matching on the interface between the load and the antenna front. In our case a plastic matching layer (0.1 mm thick) is used to improve the return loss by 4–5 dB.

The transmitting antenna design is inspired by the dual concentric conductor applicator developed by Stauffer and co-workers [10]. By setting up a rotational symmetric E-field (independent of ϕ_s , see Figure 1) from the center of the applicator to the outer ring, the resulting radiation pattern is minimized centrally along the boresight direction due to destructive interference. The outer ring itself is grounded to the back plane at four places ($\phi_s = 0, \frac{\pi}{2}, \pi, \frac{3\pi}{2}$). The electric field lines couple capacitively to ground both through the antenna dielectric and through the lossy medium. Owing to the large permittivity difference between the lossy medium ($\epsilon_m = 80$) and substrate ($\epsilon_{rs} = 2.53$), the coupling between the feed point and outer ring is expected to be the source of the dominant radiating effect. This property is confirmed by a pronounced asymmetry measured in the radiation pattern when one of the shorting pins between the outer ring and ground plane is removed.

Furthermore, maximum radiation appears somewhere between the center and the periphery (depending on antenna size to wavelength fraction) yielding a doughnut-like power distribution in the z-plane (see Figure 4d). The construction symmetry yields a circular polarized wave, which in certain anatomical locations may reduce the undesired heating of normal tissues, and improve the power deposition pattern compared to a linearly polarized configuration [28]. In the retrieval of temperature depth profiles in biological media, Hamamura et al. [29] emphasize the advantage of using two orthogonal polarizations to view the same lateral region of the object.

From the aperture shape and radiation characteristics of the applicator a descriptive name would be microstrip coplanar grounded ring antenna.

2.2 Performance indices

It is possible to define a multitude of performance factors. In order to evaluate the concept of the integrated tranceiving antenna, 4 applicator performance indices (API's) are defined. Emphasis has been placed on nearfield antenna radiation and receiving properties as well as S-parameters.

For the transmitting coplanar grounded ring antenna, relevant quantities are the effective field size (A_1) localized within the aperture boundaries, and the total effective field size (A_2); both defined according to the area encompassed by the 50% of maximum E^2_{tot} ($> 50\,\%$ SAR_{max}) in a plane at 10 mm depth [12]. The total power deposition is given by $E^2_{tot} = E^2_x + E^2_y + E^2_z$ where E^2_x, E^2_y, and E^2_z are the power distributions in three orthogonal planes of Figure 1B. A projection of the 3.5 cm diameter ring is drawn over the contour plots in Figures 4d and 5d.

Normalizing relative to the aperture size, we define:

$$API^{(1)} = \frac{A_1}{\text{Aperture Area}} \tag{1}$$

$$API^{(2)} = \frac{A_2}{\text{Aperture Area}} \tag{2}$$

Antennas providing an effective field size comparable to the aperture size yield $API^{(1)} \sim API^{(2)} \simeq 1$.

The receiving spiral antenna is required to be directive. Defining area A_3 to be the inner 25% of the aperture area (see inner circle contour of Figure 5d), the parameter:

$$API^{(3)} = \frac{A_3 - \text{Area of } [> 50\% SAR_{max} \text{ outside } A_3]}{A_3} \tag{3}$$

is a measure of directivity.

As the percentage of radiated power localized outside A_3 is increased, $API^{(3)}$ decreases toward 0, whereas a narrow beam in the boresight direction corresponds to higher $API^{(3)}$-values. The upper limit $API^{(3)} = 1.0$ is associated with the entire region between 50–100% SAR_{max} being contained within the central A_3 region of the aperture.

In the light of the elucidation on antenna size versus spatial resolution and penetration depth, we finally define the following performance

index:

$$API^{(d)} = \text{Depth at which } [A_2 = \text{Aperture Area}] \tag{4}$$

This length measures the maximum sensing depth that can be used without getting significant contribution to the received signal from adjacent resolution cells under the influence of other microwave sources.

2.3 Measurements of Antenna Performance

Different microwave tests of antenna radiation were performed in the frequency range from 800 to 2400 MHz using a network analyzer. Variations of return loss (S_{11} -parameter) versus frequency were measured to reveal coupling to a dissipative medium ($6g/$ L saline solution) simulating high water content tissues. The relative permittivity and conductivity of the phantom vary monotonically from $\epsilon_m = 77.6$ and $\sigma_m = 1.1$ S/m at 800 MHz to $\epsilon_m = 76.4$ and $\sigma_m = 2.6$ S/m at 2400 MHz, respectively.

Radiated field distributions of the transmitting and receiving antennas were measured in the dissipative medium described above. A computer controlled stepper motor based 3 axis scanning system was used to scan a passive monopole probe through the phantom in order to map E-field distributions as a function of space (0.5 mm accuracy) and frequency (40 MHz resolution). The probe was simply constructed [30] from a rigid coaxial cable (RGI141). The inner conductor, covered by a dielectric of polyethylene, extends approximately 14 mm beyond the end of the tube to expose center conductor and dielectric core. Furthermore, the coupled signal from the probe is fed to a homodyne (phase and amplitude) detection system. The sensor configuration provided a spatial resolution of 2 mm perpendicular and 14 mm along the axis of the monopole, respectively. By rotating the probe 90^0 to three orthogonal positions, a mapping of the E_x -, E_y -, and E_z -field components was obtained in three sequential procedures. For each scan the initial starting point was repeatable within ± 0.5mm. The cross-polarization damping of the probe was determined to be > 23 dB.

Radiated fields were displayed as relative power deposition (SAR) patterns assuming the relationship $SAR = \frac{\sigma_m}{2\rho_m} E_{tot}^2$ or as individual components E_x^2 , E_y^2 , and E_z^2 , where ρ_m is the density of the phantom material. Distributions were measured for the plane parallel to

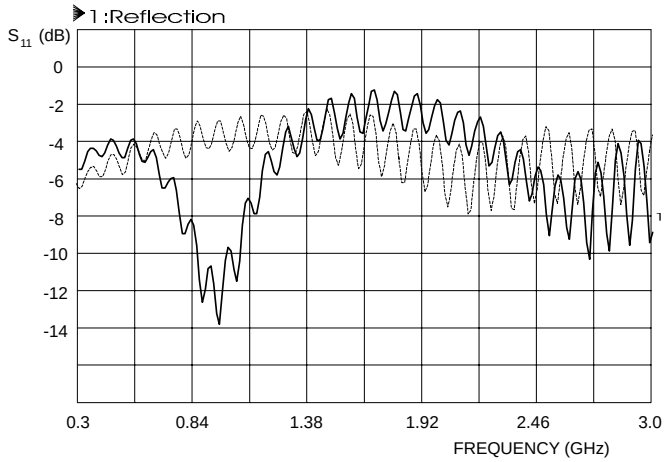

Figure 2. Return loss of coplaner grounded ring antenna, thin dashed line: without matching, thick solid line: matched to 915 MHz using stub tuning.

the applicator surface at z=1 cm depth in the phantom, and in the horizontal x-z plane cross section through the center of the aperture.

3. RESULTS

Figure 2 shows the magnitude of the reflection coefficient versus frequency for the coplanar grounded ring antenna. The coplanar grounded ring antenna is indeed not resonant and the return loss is typically -4 to -5 dB. In order to improve the efficiency some type of matching circuit can be included. Using microstrip stub tuning at a specific frequency (here 915 MHz), the quality of the matching is improved to -14 dB (4% reflected power). Note however that the antenna with stub tuning is more sensitive to variable loading than without.

Figure 3 shows a similar return loss characteristic for the central spiral antenna. The microstrip spiral antenna is extremely broadband due to its quasi-equiangular shape with the lower cutoff frequency limited by the transversal antenna dimension [31]. From Figure 3 we observe that the matching to the lossy dielectric medium is $S_{11} < -10$ dB ($< 9.5\%$ reflected power) over the entire frequency range of interest.

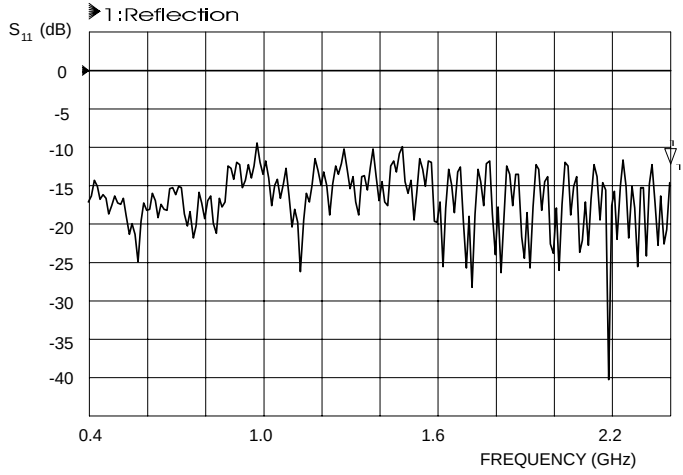

Figure 3. Return loss of microstrip spiral antenna.

Figure 4 depicts a typical relative power distribution of the coplanar grounded ring antenna for the three perpendicular polarization directions x, y, and z referenced in Figure 1. Due to symmetry, the E_x^2 component is (nearly) identical to E_y^2 except for a 90° rotation. From visual inspection we notice that the z-component is complementary to the other to polarizations filling in the centrally low E_x- and E_y-field components.

As for the microstrip spiral antenna, Figure 5 shows the corresponding radiation patterns of this element at 1600 MHz. From the antenna reciprocity theorem, the antenna receiving pattern is identical to the SAR distribution. At this specific frequency, the design criteria (narrow main lobe centered along the boresight axis) are satisfied.

To assess the overall performance of the hybrid antenna concept, the index parameters defined in Section 2.2 were calculated in the above mentioned frequency range. From Figure 6, we notice that the transmitting coplanar grounded ring antenna has an effective field size, $\mathrm{API}^{(2)}$, greater than the aperture size in the 1 cm deep plane. Due to the doughnut shape of the radiation pattern, the field size coverage $\mathrm{API}^{(1)}$ inside the aperture area is slightly less than 1 (Figure 6). As described in Section 3, the factor which limits resonance mode radiation of the microstrip spiral antenna, is the transverse dimension. The cutoff frequency of the present design is approximately 1250 MHz (Figure 7). At lower frequencies, the antenna receiving pattern be-

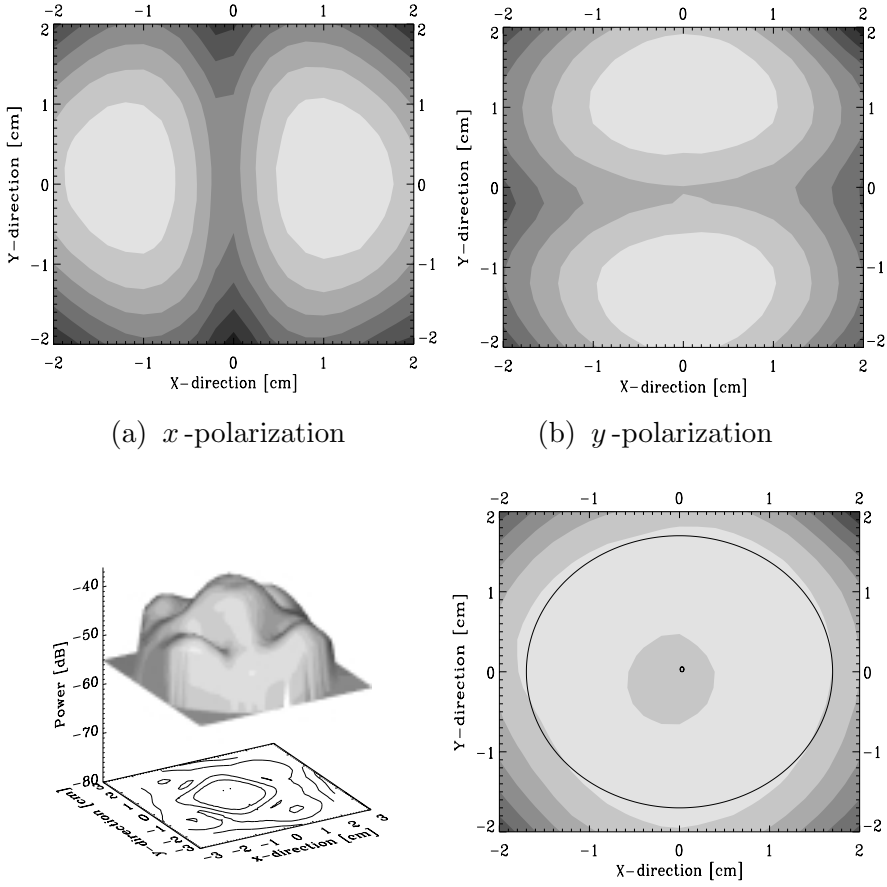

(a) x-polarization (b) y-polarization

(c) z-polarization (d) $E_{tot}^2 \propto SAR$

Figure 4. Measured power deposition pattern of coplaner grounded ring antenna 1 cm deep in muscle phantom at 1600 MHz. Contours are at 3 dB intervals. The circle is a projection of the outer ring.

comes less focused with maximum radiation occurring in broad sidelobes rather than centrally under the spiral.

Moreover, Figure 5 depicts only the receiving properties in the reactive nearfield of the $z = 1$ cm deep plane. From a thermometry point of view, deeper penetration depths are also of interest. Figure 8 shows two representative examples of $E_x^2 + E_y^2$ measured in the xz-plane in front of the antenna (the E_z^2 component is negligible at depths greater

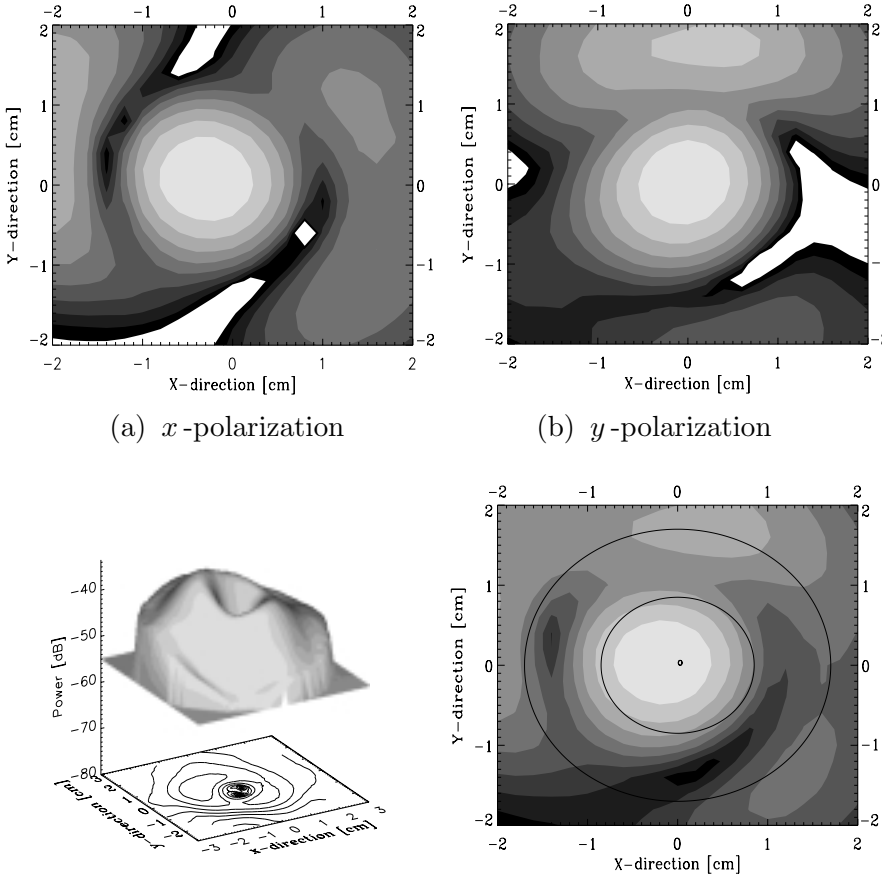

(a) x-polarization (b) y-polarization

(c) z-polarization (d) $E_{tot}^2 \propto SAR$

Figure 5. Measured power deposition pattern of microstrip spiral antenna 1 cm deep in muscle phantom at 1600 MHz. Contours are at 3 dB intervals. The inner circle delimits the A_3 area (see Equation (3)) and the outer circle is a projection of the physical aperture.

than 1 cm). The antenna is well behaved at 1600 MHz with a narrow main lobe directly in front of the antenna. At 800 MHz, however, the beam is split into two broad side lobes due to non-resonant mode radiation.

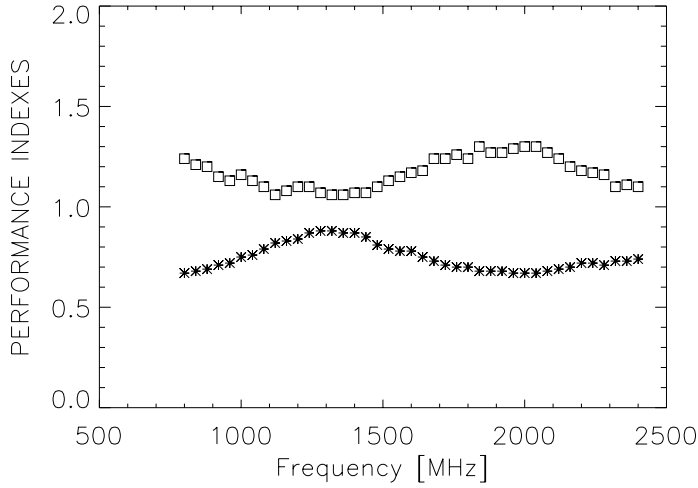

Figure 6. Calculated performance of coplaner grounded ring antenna; $(*)$: API $^{(1)}$ (Equation (1)) and $(\square)$: API $^{(2)}$ (Equation (2)).

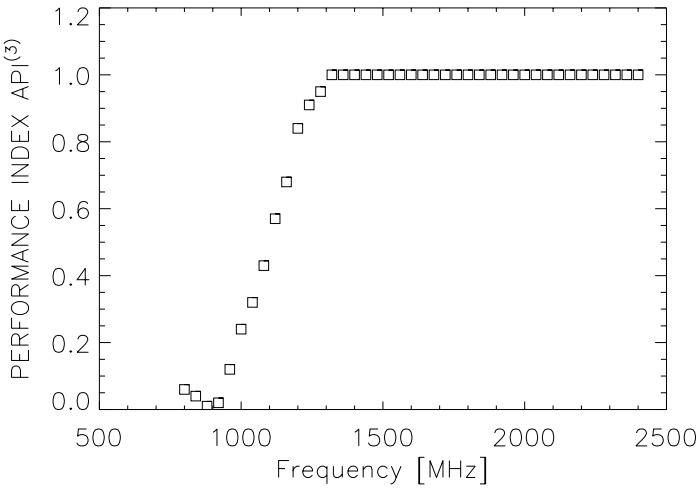

Figure 7. Calculated performance index API $^{(3)}$ (Equation (3)) of microstrip spiral antenna.

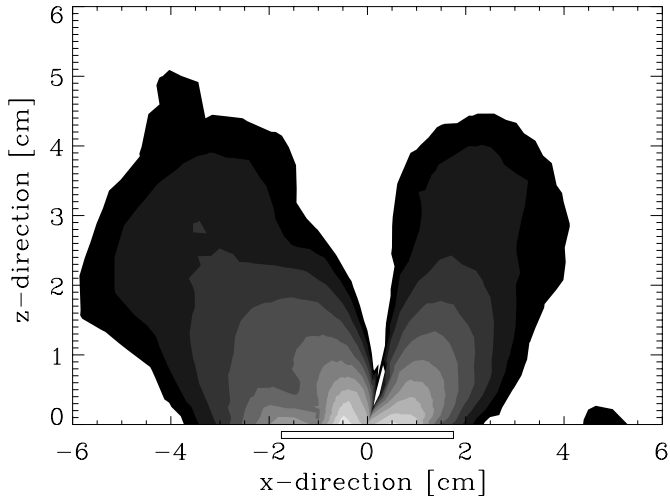

(a) $f = 800$ MHz

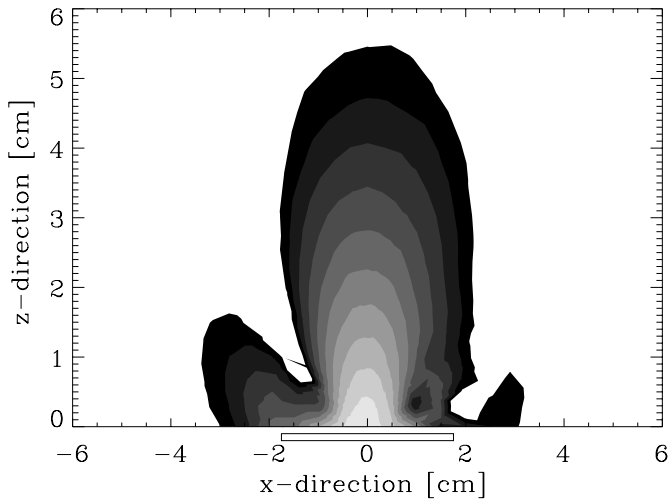

(b) $f = 1600$ MHz

Figure 8. Measured power distribution $E_x^2 + E_y^2$ of microstrip spiral antenna in xz-plane. Small rectangle is antenna extent.

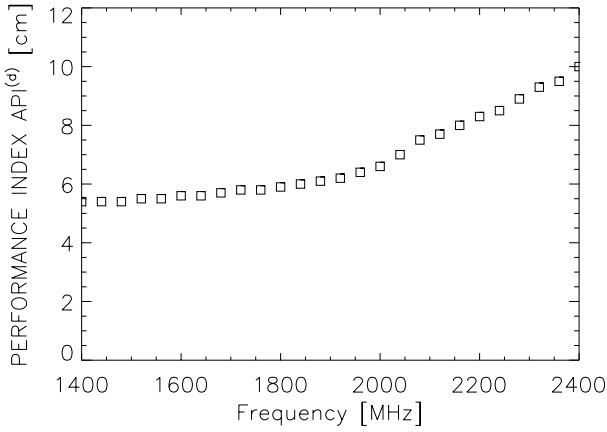

Figure 9. Calculated performance index API $^{(d)}$ (Equation(4)) of microstrip spiral antenna.

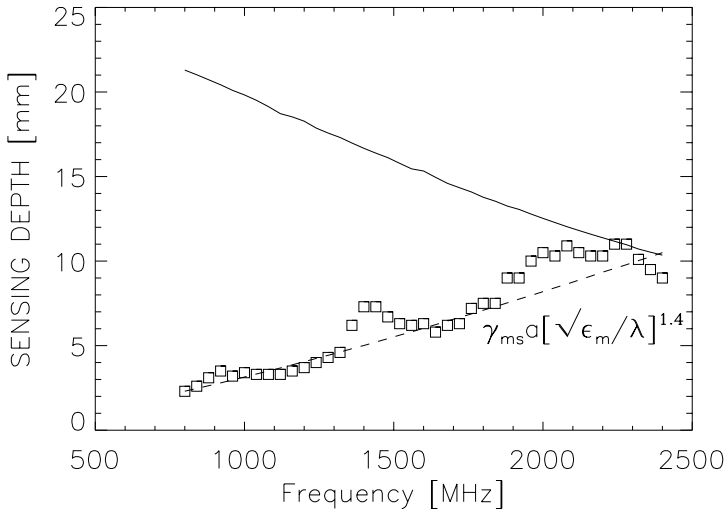

Figure 10. Calculated and modeled maximum energy sensing depth. Plane wave model (solid line), aperture model with aperture illumination efficiency γ_{ms} =0.1 and aperture width $a = 2.5$ cm (dashed line), and estimated for microstrip spiral antenna (▫) .

Equation (4) parameterizes the maximum detection depth as a function of transverse spatial resolution. This performance index was experimentally generated as a function of frequency for the given antenna size (Figure 9).

In the Introduction we emphasized that the effective depth of sensing for typical antennas applied to radiometry, is affected by the antenna dimension and geometry as well as material properties of the medium; not only determined by the plane-wave penetration depth. From the measurements in the xz-plane it is possible to determine the power density reduction along the z-axis. We consequently estimated the depth $\hat{p}_d$ where the energy deposition was decreased a factor e^{-1} from that at the aperture plane. Figure 10 quantifies this parameter in the frequency range from 800 to 2400 MHz.

4. CONCLUSION AND DISCUSSION

A new tranceiving antenna concept is introduced for simultaneous hyperthermic heating and thermometry of superficial tumors at microwave frequencies. We propose an integrated dual antenna design to accommodate conflicting design constraints for the heating and thermometry aspects of the application. The concept consists of a microstrip spiral antenna for radiometric noise signal sensing from the tissue, and a coplanar grounded ring antenna for uniform heating of tissue (Figure 1).

Two types of measurements were performed on each antenna structure. Using a network analyzer, the return loss (S_{11}-parameter) was measured in a dissipative medium (6 g/L saline solution) simulating high water content tissue. By means of stub tuning, S_{11} of the coplanar grounded ring antenna was improved from -4 dB to -14 dB at the desired heating frequency of 915 MHz. The overall quality of the matching for the radiometric microstrip spiral is given by $S_{11} < -10$ dB over a broad frequency range from 400 to 2400 MHz.

The second part of the measurements included determination of the applicator radiation patterns into the above-mentioned phantom. As quantified by API[3] in Figure 7, the microstrip spiral is directive along the boresight direction (1400–2400 MHz) since it was designed to maximize the noise sensing depth. On the contrary, we require the coplanar grounded ring antenna to be capable of generating a uniform, large area power deposition pattern. At 1 cm depth, this area is comparable to the aperture size as shown in Figure 4. Both the effective

field size and the shape of the radiation pattern are similar to results obtained by other research groups [10], [32]. Observe also the resemblance of the radiation pattern to what dual beam antennas produce [33].

In clinical use of microwave hyperthermia, printed circuit applicators have been reported to produce pain related to excessive electrical field components normal to the antenna face. For a 17-element hexagonal phased array applicator, the normal peak electric field amplitude was measured at 1 cm depth in muscle tissue to be +13.5 dB larger than the tangential component [28]. The ratio decreased with increasing depth since this phenomenon dominates in the reactive nearfield. From the E^2 distribution measurements of this paper, the normal electrical field component for the coplanar grounded ring antenna is a factor of at least -6 dB (typically -10 to -16 dB) *smaller* than the the tangential component (data not shown). Although the setups are not directly comparable, this result indicates that the potential of using a relatively thin bolus is present for the coplanar grounded ring antenna. Furthermore, the coplanar grounded ring antenna also generates a circularly polarized wave. The advantages of distributing the transmitted energy into two independent linearly polarized waves, apply to both the heating [28] and thermometry [29].

We also examined the effectiveness of the microstrip spiral in terms of sensing depth, transverse spatial resolution, frequency, and applicator size. Above 1400 MHz, the 3.5 cm diameter microstrip spiral generates a narrow beam in the $\theta = 0^\circ$ direction as shown in Figure 8. Below 1400 MHz, however, the radiation pattern becomes notably more omnidirectional and unsuitable for radiometry. While large spirals could be used to lower the cutoff frequency (approximately 600 MHz for a 6 cm diameter spiral) this is achieved at the expense of transverse spatial resolution of the physically larger antenna.

The effective sensing depth is a function of two parameters. It decreases rapidly in biological tissue with increasing frequency for plane wave and electrically large antennas. Typically the e^{-1} power penetration distance in a muscle equivalent agar phantom for a 2×1.5 cm^2 large waveguide antenna is limited to 17 mm at 1 GHz and 6 mm at 2 GHz [23]. In the latter thermometry setup, a realistic maximum sensing depth was reported to be 5 cm. Cheever [34] studied the influence of aperture size on the effective sensing depth for dielectrically loaded waveguide antennas operated at multiple frequencies. From measure-

ments in both ethanol and water media, they came up with two regimes for this parameter. i) An upper bound determined by plane-wave propagation describing electrically large antennas, ii) a lower bound dependent on antenna size and independent of tissue loss. The latter e^{-1} energy sensing depth was calculated to $p_d \simeq \gamma_w a \left[\frac{a\sqrt{\epsilon_m}}{\lambda}\right]^{1.4}$ where $\gamma_w = 0.4$, a is the aperture width, and λ is the wavelength in the lossy medium.

To evaluate the different models we measured the penetration depth $\hat{p}_d$ along the z-axis for the microstrip spiral antenna. Figure 10 reveals that the microstrip spiral antenna is electrically small and associated with an *increasing* sensing depth up to 2.3 GHz where the tissue loss starts to dominate. Above 2.3 GHz the sensing depth is close to the upper theoretical limit. The model for electrically small antennas (dashed line in Figure 10) is included for comparison of trends. Observe that the antenna size scaling factor for the microstrip spiral is γ_{ms} =0.1 compared to γ_w =0.4 for the loaded waveguide. This indicates that the aperture illumination efficiency of the microstrip spiral is smaller than for waveguide antennas.

Relating the waveguide and printed antenna sizes outlined above, and taking into account that both the performance index $API^{(d)}$ and the sensing depth $\hat{p}_d$ *increase* within a frequency span of nearly one octave, an aperture size of 2.5 cm seems reasonable.

In the lights of the merits, $API^{(1)} > 1$, $API^{(2)} \simeq 0.8$, $API^{(3)}$ =1.0 above 1400 MHz, and $API^{(d)} > 5$ cm, the presented empirical-based applicator design appears to perform acceptably in a homogeneous medium. The antenna element has the potential to represent a basic building block element for large-area array applicators with combined heating and multi- frequency radiometry.

REFERENCES

1. Masunaga, S., M. Hiraoka, M. Takahashi, S. Jo, and K. Akuta, "Clinical results of thermoradiotherapy for locally advanced and/or recurrent breast cancer-comparison of results with radiotherapy alone," *Int. Journal of Hyperthermia,* Vol. 6, No. 3, 487–497, 1990.
2. Anderson, R. L., and D. S. Kapp, "Hyperthermia in cancer therapy, current status," *Medical Journal Australia,* Vol. 152, 310–315, 1990.

3. Kapp, D., R. Cox, T. Barnett, and R. Ben-Yosef, "Thermoradiotherapy for residual microscopic cancer: Elective or post-excisional hyperthermia and radiation therapy in the management of local-regional recurrent breast cancer," *Int. Journal of Radiation Oncology Biology Physics,* Vol. 24, No. 2, 261–277, 1992.
4. Bahl, I. J., and M. A. Stuchly, "A new microstrip radiator for medical applications," *Electronic Letters,* 16, 731–732, 1980.
5. Ledee, R., M. Chive, and M. Plancot, "Microstrip microslot antennas for biomedical applications: frequency analysis of different parameters of this type of applicator," *Electronic Letters,* Vol. 21, 304–305, 1985.
6. Beyne, L., and D. DeZutter, "Power deposition of a microstrip applicator radiating into a layered biological structure," *IEEE. Trans. on Microwave Theory and Techniques,* MTT-36, 126–131, 1988.
7. Montecchia, F., "Microstrip-antenna design for hyperthermia treatment of superficial tumors," *IEEE Trans. on Biomedical Engineering,* Vol. 39, No. 6, 580–588, 1992.
8. Lee, E. R., T. R. Wilsey, P. T. Hornoch, D. S. Kapp, P. Fessenden, A. Lohrbach, and S. D. Prionas, "Body Conformable 915 MHz Microstrip Array Applicators for Large Surface Area Hyperthermia," *IEEE Trans. on Biomedical Engineering,* Vol. 39, No. 5, 470–483, 1992.
9. Samulski, T. V., P. Fessenden, E. R. Lee, D. S. Kapp, E. Tanabe, and A. McEuen, "Spiral microstrip hyperthermia applicators: Technical design and clinical performance," *Int. Journal of Radiation Oncology Biology Physics,* Vol. 18, No. 1, 233-242, 1990.
10. Stauffer, P. R., M. Leoncini, V. Manfrini, G. B. Gentili, C. J. Diederich, and D. Bozzo, "Dual concentric conductor radiator for microwave hyperthermia with improved uniformity to periphery of aperture," *IEICE Trans. Communication,* Vol. E78-B, No. 6, 826–834, June 1995.
11. Dubois, L., J. Pribetich, J. J. Fabre, M. Chive, and Y. Moschetto, "Non-invasive microwave multifrequency radiometry used in microwave hyperthermia for bidimensional reconstruction of temperature patterns," *Int. Journal of Hyperthermia,* Vol. 9, No. 3, 415–431, 1993.

12. Prior, M. V., M. L. D. Lumiori, J. W. Hand, G. Lamaitre, C. J. Schneider, and J. D. P. Dijk, "The use of a current sheet applicator array for superficial hyperthermia: Incoherent Versus coherent operation," *IEEE Trans. on Biomedical Engineering,* Vol. 42, No. 7, 694–698, 1995.
13. Christensen, D. A., and C. H. Durney, "Hyperthermia production for cancer therapy: A review of fundamentals and methods," *Journal of Microwave Power,* Vol. 16, No. 2, 89–105, 1981.
14. Seip, R., and E. S. Ebbini, "Noninvasive Estimation of Tissue Temperature Response to Heating Fields Using Diagnostic Ultrasound," *IEEE Trans. on Biomedical Engineering,* Vol. 42, No. 8., 828-839, 1995.
15. Paulsen, K. D., J. Moskowittz, T. P. Ryan, and S. E. Mitchell, "Temp field estimation using electric impedance profiling methods. I. Reconstruction algorithm and simulated results," *Int. Journal of Hyperthermia,* Vol. 10, No. 2, 209–228, 1994.
16. Moskowitz, M. J., K. D. Paulsen, and T. P. Ryan, "Temp. field estimation using electrical impedance profiling methods. II. Experimental system description and phantom results," *International Journal of Hyperthermia,* Vol. 10, No. 2, 229–245, 1994.
17. Chang, J. T., K. D. Paulsen, and P. M. Meaney, "Active microwave imaging for noninvasive temperature sensing: initial experimental results," *Proceedings of the 7th International Congress on Hyperthermic Oncology,* ed: C. Franconi, G. Arcangeli and R. Cavaliere, 430–432, Rome, Italy April 9-13, 1996.
18. Wust, P., P. Konstanczak, B. Sander, V. Knappe, S. Scründer, W. Wlodarczyk, T. Frenzel, G. Müller, and R. Felix, "Noninvasive thermometry performed my measuring the chemical shift of lanthanide complex," *Proceedings of the 7th International Congress on Hyperthermic Oncology,* ed: C. Franconi, G. Arcangeli and R. Cavaliere, 436–438, Rome, Italy April 9–13 1996.
19. Barret, A. H., and P. C. Myers, "Subcutaneous temperatures: A method of noninvasive sensing," *Science,* Vol. 190, 669–671, 1975.
20. Enander, B., and G. Larson, "Microwave radiometry measurements of the temperature inside a body," *Electronic Letters,* Vol. 10, 317, 1974.
21. Chivé, M., M. Plancot, G. Giaux, and B. Prevost, "Microwave hyperthermia controlled by microwave radiometry: Technical aspects and first clinical results," *Journal of Microwave Power,* Vol. 19, No. 4, 233–241, 1984.
22. Cheever, E. A., and K. R. Foster, "Microwave radiometry in living tissue: What does it measure?," *IEEE Trans. on Biomedical Engineering,* Vol. 39, No. 6, 563–568, 1992.

23. Mizushina, S., T. Shimuzu, K. Suzuki, M. Kinomura, H. Ohba, and T. Sugiura, "Retrieval of temperature-depth profiles in biological objects from multi-frequency microwave radiometric data," *Journal of Electromagnetic Waves and Applications,* Vol. 7, No. 11, 515–1548, 1993.
24. Enel, L., Y. Leroy, J. C. van de Velde, and A. Momouni, "Improved recognition of thermal structures by microwave radiometry," *Electronic Letters,* Vol. 20, No. 7, 293–294, 1984.
25. Leroy, Y., A. Mamouni, J. C. van de Velde, B. Bocquet, and B. Dujardin, "Microwave radiometry for non-invasive thermometry," *Automedica,* Vol. 8, 181–202, 1987.
26. Montecchia, F., "The design and evaluation of superficial hyperthermia applicators using microstrip technology," *Physical Medica,* Vol. 5, Suppl. 1, 271–274, 1989.
27. Wang, J. J. H., and V. K. Tripp, "Design of multioctave spiral-mode microstrip antennas," *IEEE Trans. on Antennas and Propagation,* Vol. 39, No. 3, 332–335, 1991
28. Magin, R. L., and F. Peterson, "Noninvasive microwave phased arrays for local hyperthermia: a review," *Int. Journal of Hyperthermia,* Vol. 5, No. 4, 429–450, 1989.
29. Hamamura, Y., S. Mizushina, and T. Sugiura, "Non-invasive measurement of temperature-versus-depth profile in biological systems using a multiple-frequency-band microwave radiometer system," *Automedica,* Vol. 8, No. 4, 213–232, 1987.
30. James, J. R., and P. S. Hall, *Handbook of Microstrip Antennas,* Peter Peregrinius, Vol. 2, 1989.
31. Johnson, R. C., *Antenna Engineering Handbook,* McGraw-Hill Inc, 1993.
32. Lédée, R., E. Playez, M. Chivé, and K. Ben Naoum, "Microstrip microslot multi-applicator for microwave hyperthermia and radiometry," *Proceedings IEEE-EMBS, 8th Annual Conference,* Fort Worth, USA, 1429–1431, 1986.
33. Zürcher, J.-F., and F. E. Gardiol, *Broadband Patch Antennas,* Artech House, 1995.
34. Cheever, E., J. B. Leonard, and K. R. Foster, "Depth of penetration of fields from rectangular apertures into lossy media," *IEEE Transactions on Microwave Theory and Techniques,* Vol. MTT-35, No. 9, 1987.